Supplementary Information

Title: "Complex Refractive Index, Single Scattering Albedo, and Mass Absorption Coefficient of Secondary Organic Aerosols Generated from Oxidation of Biogenic and Anthropogenic Precursors"

Justin H. Dingle [1], Stephen Zimmerman [2], Alexander L. Frie [2], Justin Min [3], Heejung Jung [4], Roya Bahreini [1,2,3]
[1] Environmental Toxicology Program, University of California, Riverside, California, USA
[2] Environmental Sciences Department. University of California, Riverside, California, USA
[3] Chemistry Department, University of California, Riverside, California, USA
[4] Mechanical Engineering Department, University of California, Riverside, California, USA

Chamber Setup and Instrumentation

The biogenic and anthropogenic hydrocarbons used in this study were longifolene (MP Biomedicals-Solon, OH, U.S.A.), α-pinene (Sigma-Aldrich-Saint Louis, MO, U.S.A., ≥99%), 1-methylnaphthalene (Sigma-Aldrich-Saint Louis, MO, U.S.A., 95%), phenol (Acros Organics-Fair Lawn, NJ, U.S.A., 99%), and toluene (OmniSolv- Billerica, MA, U.S.A, 99.99%). All experiments were conducted in a 2 m^3 PFA Teflon chamber bag, enclosed by a metallic frame, irradiated by 16 Sylvannia black lights under relative humidity ranging from 20-30% (Vaisala, HMP60 Series relative humidity and temperature probe) at temperatures between 22-25 °C.

The experiments used either the photolysis of hydrogen peroxide (H_2O_2, Sigma-Aldrich-Saint Louis, MO, U.S.A., 50 % wt. in water) or nitrous acid (HONO) as the hydroxyl radical source (OH) for intermediate- and high-NO_x conditions, respectively. For intermediate-NO_x experiments, ~75 µl of H_2O_2 was evaporated into the chamber. For high-NO_x conditions, HONO was produced by dropwise addition of 150 µl sulfuric acid (Fluka Analytical-Gillman, SA, Aus, 13 mM) in a bulb, containing ~0.67 ml sodium nitrite (Fluka Analytical-Gillman, SA, Aus, 1 M). In experiments with HONO as the OH source, additional NO (PRAXAIR, 484 ppm) was also injected into the chamber to achieve initial NO mixing ratios of ~500 ppbv in the chamber. In all experiments, hexafluorobenzene (Sigma-Aldrich-Saint Louis, MO, U.S.A., 99%) was added as a tracer to determine the dilution rate in the chamber. Hydrocarbons were injected by flowing zero air over a specific volume of the hydrocarbon liquid sample in a glass bulb. Gas phase concentrations of the hydrocarbon were measured with Gas Chromatography coupled with a Flame Ionizing Detector (GC-FID) using a Hewlett Packard 5890 Series II and DB-5 (0.25 mm I.D. x 30 m, 0.25 µm film thickness, (5% phenyl-Agilent) column. The response of the GC-FID

to each hydrocarbon was calibrated by injecting known amounts of the hydrocarbon into a small Teflon bag.

To determine OH concentrations in the chamber, experiments were performed where H_2O_2 or HONO+NO injections were followed by injection of octane (Sigma-Aldrich-Saint Louis, MO, U.S.A., 99%). Once hydrocarbon gas phase concentrations were stable, black lights were turned on, and the decay of octane and C_6F_6 was monitored for 3-4 hours. Considering the OH reaction rate constant of octane and its dilution corrected concentrations, average OH concentrations of the H_2O_2 (intermediate-NO_x) and HONO (high-NO_x) experiments were measured as 6.3×10^6 molecules cm^{-3} and 3.6×10^7 molecules cm^{-3}, respectively.

In SOA formation experiments, after injection of the OH source, the hydrocarbon of interest and C_6F_6 were injected, and the GC-FID monitored their concentrations. For intermediate-NO_x systems with H_2O_2 as the OH source, high and low hydrocarbon concentrations were tested. For high-NOx systems with HONO as the OH source, only high hydrocarbon concentrations were tested.

Polydispersed dry ammonium sulfate and carbon black (Cabot Corp.-Negeri, Sembilan, Malaysia, R400R) aerosols were used to calibrate for β_{scat} and β_{abs} components of PAX, respectively (Nakayama et al. 2015). Dry ammonium sulfate was used to obtain extinction from a purely scattering material. Since ammonium sulfate is a purely scattering material, a 1:1 relationship between the calculated β_{ext} and measured β_{scat} is expected. The intensities of laser light reaching the detector during filter and ammonium sulfate measurements were recorded and applied to Beer-Lambert Law in equation S1 to determine the calculated β_{ext}:

$$\beta_{ext} = -\frac{1}{L} * ln\frac{I}{I_o} * 10^6 \ (Mm^{-1}) \qquad \text{(S1)}$$

where β_{ext} is the calculated extinction coefficient at 375 nm, L is the path length (m) of the laser beam in the system's sampling cavity at a value of 0.354 m, I_o is the radiation intensity during filter sampling time, and I is the radiation intensity during sampling of ammonium sulfate. The slope of a linear regression fit to the calculated β_{ext} against the measured β_{scat} was used as the correction factor to the scattering calibration factor of the system. Similarly, the process above was repeated to calibrate the absorption component of the measurement, using carbon black. The calculated β_{ext} was obtained again using the Beer-Lambert Law from equation S1, while the measured β_{scat} was subtracted from the calculated β_{ext} to obtain the calculated β_{abs}. The slope of the calculated β_{abs} against measured β_{abs} was used to correct the absorption calibration factor.

Sizing accuracy of the SEMS was determined to be ~ ± 3% by comparing the mode of the measured size distributions when sampling 90 nm, 150 nm, 300 nm, 500 nm, and 700 nm standard polystyrene latex sphere standards (Polysciences, Inc.-Warrington, PA, U.S.A). Counting accuracy of the SEMS is expected to be better than ~ ± 10% (Personal communication, Brechtel Manufacturing Inc.).

Single Scattering Albedo (SSA) Calculations

We measured the single scattering albedo (SSA) of the SOA products using the Photoacoustic Extinctiometer (PAX) at 375 nm. SSA is defined as the ratio of light scattering to total light extinction ($\beta_{scat} + \beta_{abs}$) in Equation S2, and is another important property to consider for climate forcing calculations (Langridge et al. 2012, McComiskey et al. 2008).

$$SSA = \frac{\beta_{scat}}{\beta_{scat}+\beta_{abs}} \quad \text{(S2)}$$

Due to size dependence of SSA, we explored the evolution of SSA in the experiments as a function of size parameter, defined as the following, (Moosmüller and Arnott 2009):

$$x = \frac{\pi d}{\lambda} \quad \text{(S3)}$$

where *d* represents the mode of the size distribution from SEMS and λ refers to the wavelength of radiation (375 nm for this setup). The relative uncertainties of the measured SSA were calculated by propagating errors in the measured β_{scat} and β_{abs} (4.5% and 6%, respectively). We determined that the relative uncertainties of SSA varied within 5.8-6.3% at different times of the experiments.

Mass Absorption Coefficient (MAC) Calculations

Using SOA mass concentrations based on the SEMS integrated volume distributions and estimates of average effective density in each experiment, we calculated the bulk mass absorption coefficient (MAC), i.e., mass-normalized value of β_{abs} at 375 nm. Effective densities were determined by comparing the SEMS volume distributions as a function of mobility diameter and mAMS mass distributions as a function of vacuum aerodynamic diameter, at several times during an experiment (Bahreini et al. 2005, DeCarlo et al. 2004). The calculated effective densities were 1.31 ± 0.08 g cm^{-3} and 1.52 ± 0.03 g cm^{-3} for 1-methylnaphthalene SOA particles under high- and intermediate-NO_x conditions, respectively. Effective densities for longifolene and phenol mixture experiments were 1.21 ± 0.05 g cm^{-3} and 1.21 ± 0.10 g cm^{-3} under high- and intermediate-NO_x conditions, respectively.

Refractive Index Calculations

To establish the applicability of the RI determination method, we applied it to compounds with known values of RI, e.g., ammonium sulfate (Thermo Scientific-Fair Lawn, NJ, U.S.A, 99.7 %) and nigrosin (Sigma-Aldrich-Saint Louis, MO, U.S.A.). Polydispersed ammonium sulfate aerosols were generated by a Collison type atomizer and dried with a silica-gel diffusion dryer before being sampled by SEMS, PAX, CAPS-PM_{ex}, and Centrifugal Particle Mass Analyzer (CPMA, Cambustion). We performed the Mie calculations and determined the refractive index of n=1.51-1.53 (χ^2=0.36-0.97) for ammonium sulfate aerosols, which is in good agreement with the reference RI value of 1.53 (Macdonald and Lide 2003, Toon et al. 1976). Similarly, the refractive index of dry, polydispersed nigrosin was determined to be (1.58-1.59) + (0.103-0.104)i at 375 nm (χ^2=0.45-0.63). Bluvshtein et al. (2017) performed wavelength-dependent RI retrievals for nigrosin using Spectroscopic ellipsometer measurements and determined that at λ=375 nm, n and k were 1.659 and 0.143, respectively, which are ~4% and 27% higher than our estimates, respectively. Ugelow et al. (2017) performed RI retrievals using photoacoustic spectroscopy and cavity ring-down spectroscopy (CASCaRD) techniques at 405 nm for nigrosin dye and estimated n=1.57 ± 0.03 and k=0.133 ± 0.014; these values are 3.3% and 14% lower than estimates of Bluvshtein et al. (2017) at λ=405 nm. One reason for differences in n and k values may be the non-standard nature of nigrosin dye that it is not a pure molecule itself but a mixture of dyes, resulting in different 'blackness' of the dye in different sample batches.

Having established the validity of our approach to estimate RI values, we applied this technique to determine time-dependent RI values of SOA particles. Figure S1 presents examples of contour plots of k vs. n, color-coded to the log of the χ^2 values, during different oxidation stages of 1-methylnaphthalene by OH radicals. In this particular case, the minimized χ^2 values

were at 0.0017, 0.0071, 0.49, and 0.066, respectively. Generally, χ^2 >>1 indicates unacceptable agreement between the measured and calculated optical coefficients while χ^2 <1 indicates satisfactory agreement (Taylor 1997). Once the optimized *n* and *k* values were determined based on the minimized values of χ^2 calculations, the corresponding calculated β_{scat} and β_{abs} at 375 nm and β_{scat} at 632 nm were compared with the measured values to further examine the closure between the measured and calculated optical coefficients. These comparisons indicated that the closure was within ~ ± 10% for β_{scat} and ± 15% for β_{abs} in each experiment, with strong correlation coefficients (r^2 >0.73).

Supplementary Table

	Refractive index (m = *n*-*ki*)						
	n (375 nm)		*k* (375 nm)		*n* (632 nm)		
Hydrocarbon	Initial	Final	Initial	Final	Initial	Final	Plot Ref.[a]
Lgf	$1.49^{+0.07}_{-0.06}$	$1.45^{+0.08}_{-0.07}$	$0.000^{+0.001}_{-0.000}$	$0.000^{+0.001}_{-0.001}$	$1.46^{+0.09}_{-0.08}$	$1.49^{+0.08}_{-0.07}$	I
Lgf	$1.49^{+0.08}_{-0.06}$	$1.48^{+0.08}_{-0.07}$	$0.000^{+0.001}_{-0.000}$	$0.000^{+0.001}_{-0.000}$	$1.46^{+0.10}_{-0.08}$	$1.48^{+0.08}_{-0.07}$	II
Lgf	$1.50^{+0.08}_{-0.06}$	$1.50^{+0.09}_{-0.07}$	$0.002^{+0.001}_{-0.000}$	$0.002^{+0.001}_{-0.000}$	$1.46^{+0.09}_{-0.08}$	$1.47^{+0.09}_{-0.07}$	III
Lgf	$1.51^{+0.08}_{-0.06}$	$1.49^{+0.09}_{-0.07}$	$0.001^{+0.001}_{-0.000}$	$0.002^{+0.000}_{-0.001}$	$1.46^{+0.09}_{-0.08}$	$1.45^{+0.08}_{-0.07}$	IV
α-P	$1.47^{+0.08}_{-0.06}$	$1.44^{+0.08}_{-0.05}$	$0.002^{+0.003}_{-0.000}$	$0.002^{+0.002}_{-0.001}$	$1.45^{+0.09}_{-0.07}$	$1.46^{+0.09}_{-0.07}$	I
α-P	$1.46^{+0.08}_{-0.05}$	$1.47^{+0.07}_{-0.06}$	$0.001^{+0.002}_{-0.001}$	$0.002^{+0.001}_{-0.001}$	$1.45^{+0.09}_{-0.07}$	$1.47^{+0.09}_{-0.07}$	II
α-P	$1.47^{+0.07}_{-0.06}$	$1.40^{+0.07}_{-0.05}$	$0.001^{+0.001}_{-0.000}$	$0.002^{+0.001}_{-0.001}$	$1.45^{+0.09}_{-0.07}$	$1.45^{+0.08}_{-0.07}$	III
α-P	$1.48^{+0.00}_{-0.06}$	$1.44^{+0.07}_{-0.06}$	$0.001^{+0.000}_{-0.001}$	$0.000^{+0.001}_{-0.001}$	$1.46^{+0.09}_{-0.07}$	$1.45^{+0.08}_{-0.07}$	IV
1-MN	$1.47^{+0.08}_{-0.07}$	$1.44^{+0.07}_{-0.06}$	$0.002^{+0.001}_{-0.000}$	$0.004^{+0.001}_{-0.001}$	$1.48^{+0.04}_{-0.09}$	$1.45^{+0.04}_{-0.08}$	I
1-MN	$1.52^{+0.09}_{-0.08}$	$1.46^{+0.07}_{-0.06}$	$0.004^{+0.002}_{-0.001}$	$0.007^{+0.001}_{-0.002}$	$1.47^{+0.04}_{-0.09}$	$1.43^{+0.11}_{-0.09}$	II
1-MN	$1.49^{+0.09}_{-0.07}$	$1.46^{+0.08}_{-0.05}$	$0.004^{+0.001}_{-0.001}$	$0.006^{+0.002}_{-0.001}$	$1.45^{+0.11}_{-0.08}$	$1.42^{+0.09}_{-0.07}$	III
1-MN	$1.48^{+0.09}_{-0.07}$	$1.46^{+0.08}_{-0.06}$	$0.001^{+0.001}_{-0.000}$	$0.007^{+0.002}_{-0.001}$	$1.48^{+0.12}_{-0.09}$	$1.44^{+0.09}_{-0.07}$	IV
1-MN	$1.55^{+0.10}_{-0.08}$	$1.55^{+0.09}_{-0.07}$	$0.013^{+0.004}_{-0.003}$	$0.017^{+0.004}_{-0.003}$	$1.52^{+0.13}_{-0.10}$	$1.50^{+0.11}_{-0.09}$	V
1-MN	$1.55^{+0.11}_{-0.09}$	$1.55^{+0.09}_{-0.07}$	$0.016^{+0.005}_{-0.004}$	$0.018^{+0.005}_{-0.003}$	$1.52^{+0.11}_{-0.08}$	$1.51^{+0.11}_{-0.08}$	VI
Phe	$1.41^{+0.07}_{-0.05}$	$1.42^{+0.07}_{-0.06}$	$0.003^{+0.001}_{-0.001}$	$0.005^{+0.001}_{-0.001}$	$1.49^{+0.11}_{-0.08}$	$1.51^{+0.09}_{-0.08}$	I
Phe	$1.45^{+0.07}_{-0.06}$	$1.45^{+0.09}_{-0.07}$	$0.003^{+0.001}_{-0.001}$	$0.005^{+0.001}_{-0.001}$	$1.46^{+0.10}_{-0.08}$	$1.48^{+0.08}_{-0.07}$	II
Phe	$1.47^{+0.09}_{-0.07}$	$1.45^{+0.09}_{-0.06}$	$0.004^{+0.003}_{-0.000}$	$0.006^{+0.002}_{-0.002}$	$1.50^{+0.10}_{-0.08}$	$1.53^{+0.09}_{-0.08}$	III
Phe	$1.50^{+0.08}_{-0.07}$	$1.45^{+0.09}_{-0.07}$	$0.004^{+0.001}_{-0.001}$	$0.012^{+0.002}_{-0.002}$	$1.46^{+0.09}_{-0.07}$	$1.46^{+0.08}_{-0.06}$	IV
Phe	$1.49^{+0.08}_{-0.07}$	$1.49^{+0.10}_{-0.07}$	$0.006^{+0.002}_{-0.002}$	$0.013^{+0.002}_{-0.002}$	$1.46^{+0.09}_{-0.07}$	$1.47^{+0.09}_{-0.07}$	V
Tol	$1.48^{+0.07}_{-0.07}$	$1.41^{+0.08}_{-0.06}$	$0.001^{+0.000}_{-0.001}$	$0.001^{+0.001}_{-0.000}$	$1.51^{+0.09}_{-0.08}$	$1.49^{+0.09}_{-0.07}$	I
Tol	$1.44^{+0.07}_{-0.06}$	$1.38^{+0.07}_{-0.05}$	$0.001^{+0.001}_{-0.000}$	$0.002^{+0.000}_{-0.001}$	$1.49^{+0.09}_{-0.08}$	$1.48^{+0.09}_{-0.07}$	II
Tol	$1.46^{+0.06}_{-0.07}$	$1.49^{+0.12}_{-0.06}$	$0.007^{+0.000}_{-0.002}$	$0.005^{+0.003}_{-0.000}$	$1.46^{+0.10}_{-0.08}$	$1.56^{+0.10}_{-0.09}$	III
Tol	$1.45^{+0.08}_{-0.06}$	$1.46^{+0.12}_{-0.07}$	$0.001^{+0.000}_{-0.001}$	$0.001^{+0.000}_{-0.000}$	$1.49^{+0.10}_{-0.08}$	$1.51^{+0.10}_{-0.08}$	IV
Tol	$1.50^{+0.08}_{-0.06}$	$1.47^{+0.08}_{-0.07}$	$0.002^{+0.001}_{-0.000}$	$0.003^{+0.000}_{-0.001}$	$1.47^{+0.09}_{-0.07}$	$1.44^{+0.08}_{-0.07}$	V
Tol	$1.45^{+0.07}_{-0.06}$	$1.44^{+0.07}_{-0.06}$	$0.006^{+0.001}_{-0.001}$	$0.006^{+0.001}_{-0.002}$	$1.44^{+0.09}_{-0.07}$	$1.46^{+0.08}_{-0.07}$	VI

Table S1. The RI values listed are the first (40-90 min after start of reaction) and last (210-378 min after start of reaction) measurement of each experiment along with their associated uncertainties.

[a]Plot reference number refers to the experiments mentioned in Table 1.

Supplementary Figures

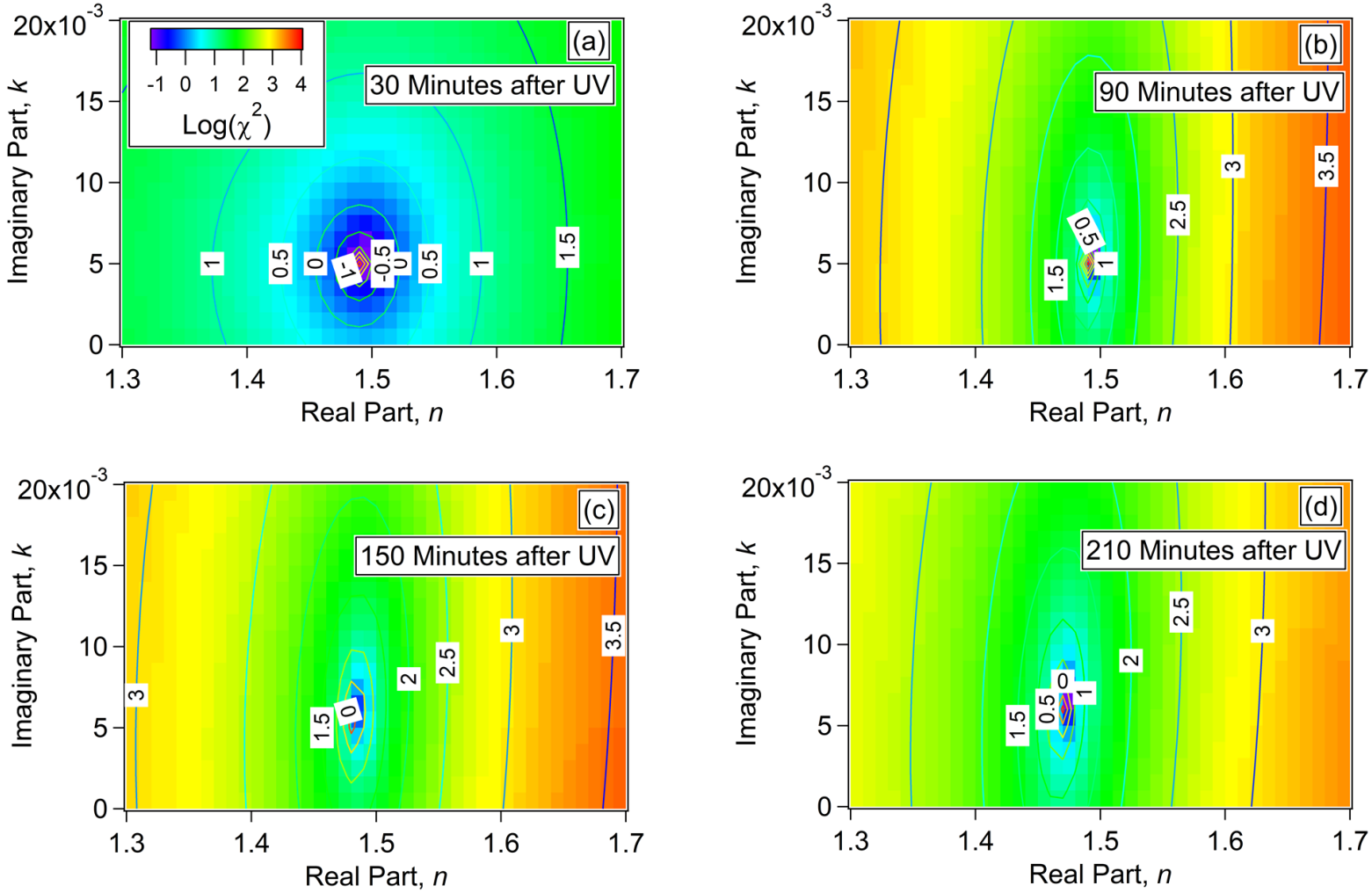

Figure S1. Sample contour plots of k vs. n, color-coded with log (χ^2), for a 1-methylnaphthalene oxidation experiment (reference plot III-Intermediate NO_x conditions) at 30, 90, 150, and 210 minutes after initiation of the experiment. Note that the colder colors indicate lower values of χ^2 and thus more optimized values of n and k.

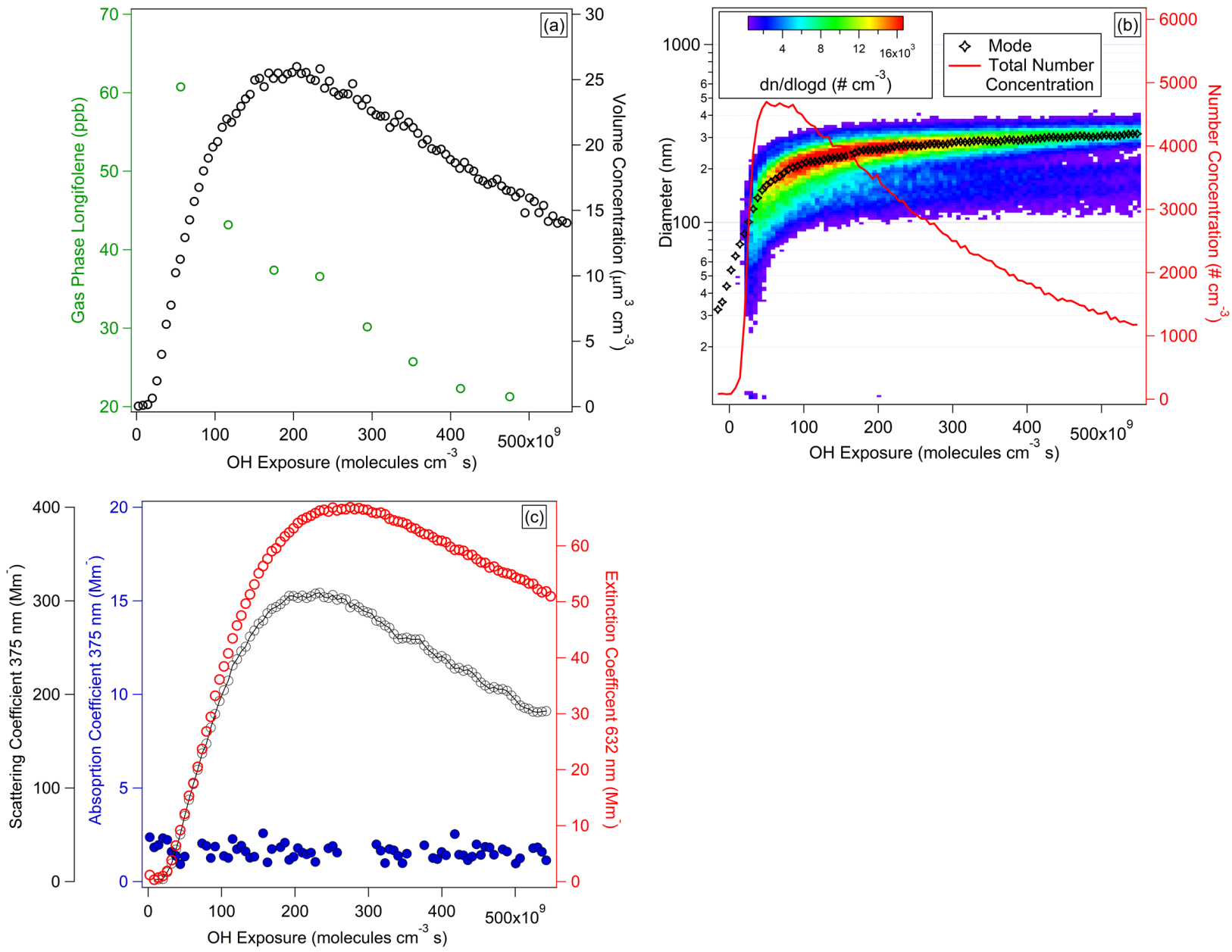

Figure S2. Time series of longifolene experiment with an initial concentration of ~86 ppbv. (a) Gas phase concentration of longifolene and SOA volume concentration, (b) SOA total particle number concentration and size distribution, (c) aerosol scattering and absorption coefficients at 375 nm and extinction coefficient at 632 nm.

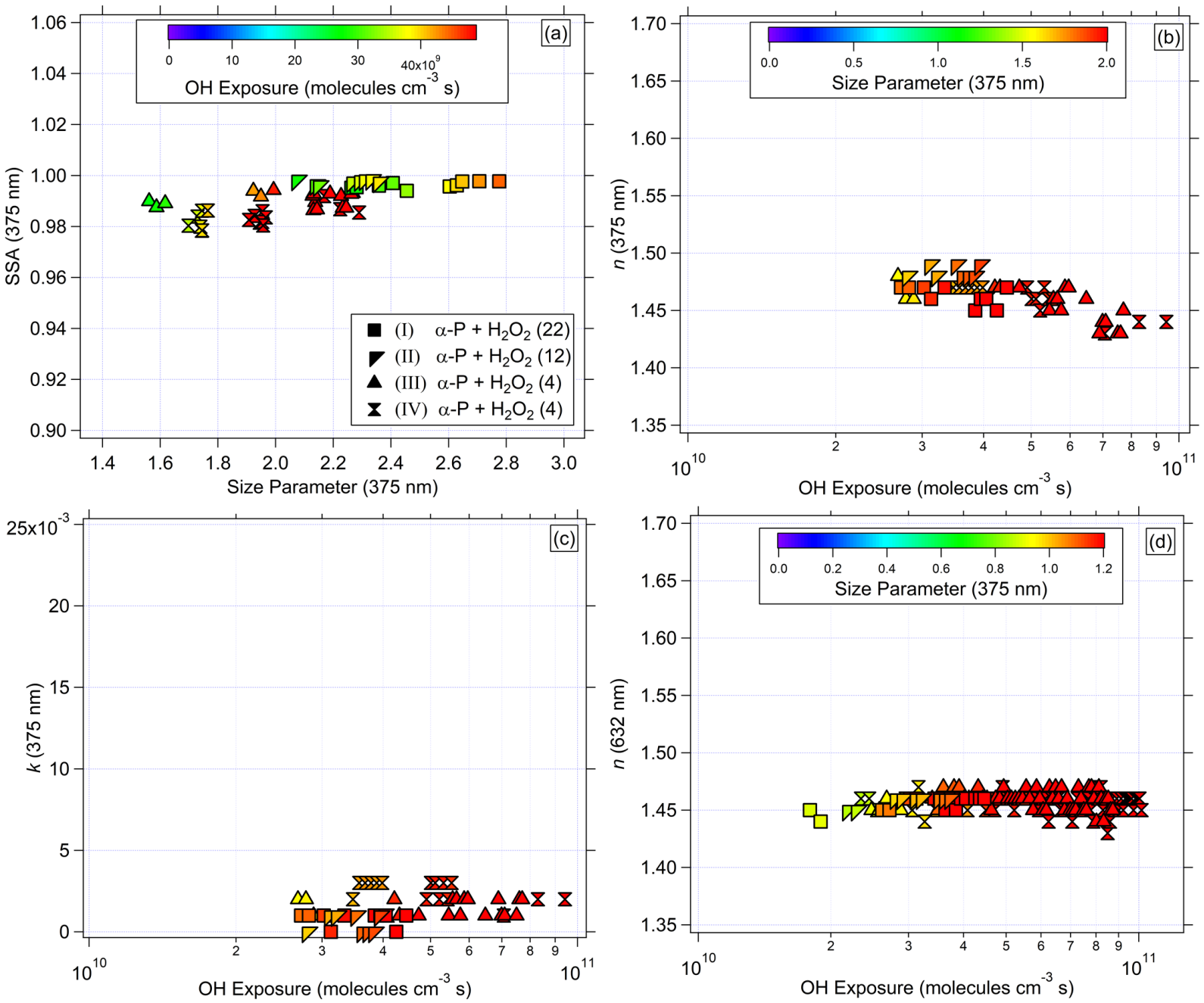

Figure S3. (a) SSA vs. size parameter, and (b) *n* at 375 nm, (c) *k* at 375 nm, and (d) *n* at 632 nm vs. OH exposure for α-pinene SOA particles.

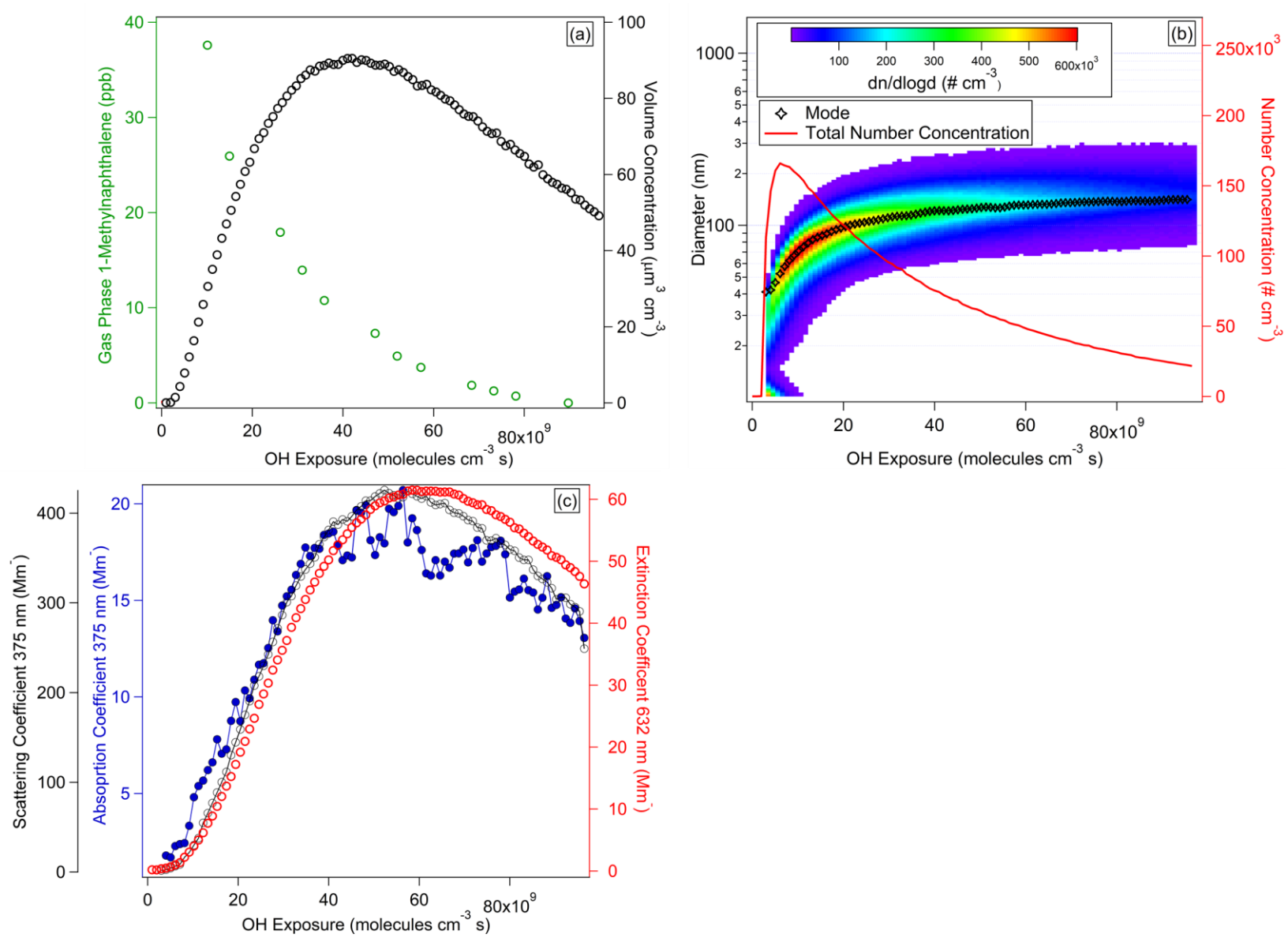

Figure S4. Time series of 1-methylnaphthalene oxidation for reference experiment III with an initial concentration of ~54 ppbv. (a) Gas phase concentration of 1-methylnaphthalene and SOA volume concentration, (b) SOA total particle number concentration and size distribution, and (c) aerosol scattering and absorption coefficients at 375 nm and extinction coefficient at 632 nm.

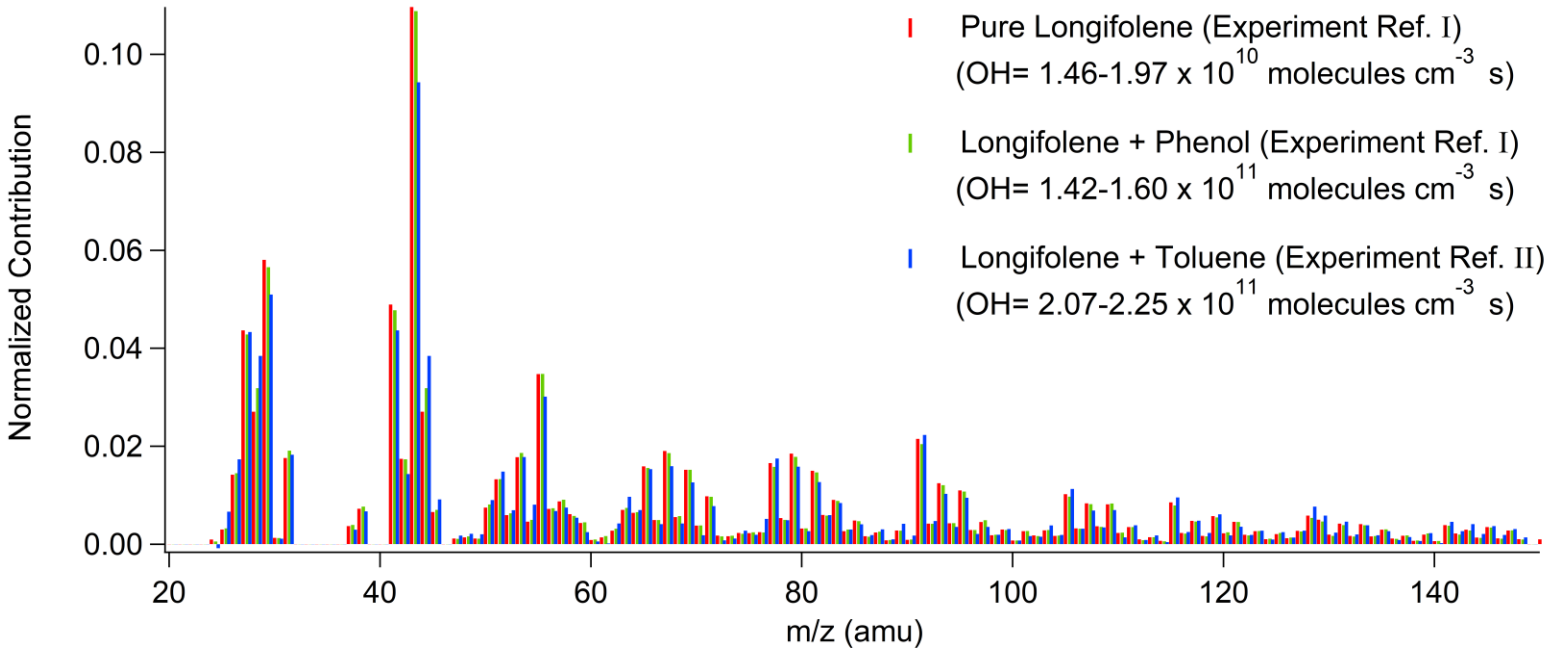

Figure S5. Mass spectra of longifolene, longifolene+phenol, and longifolene+toluene SOA particles.

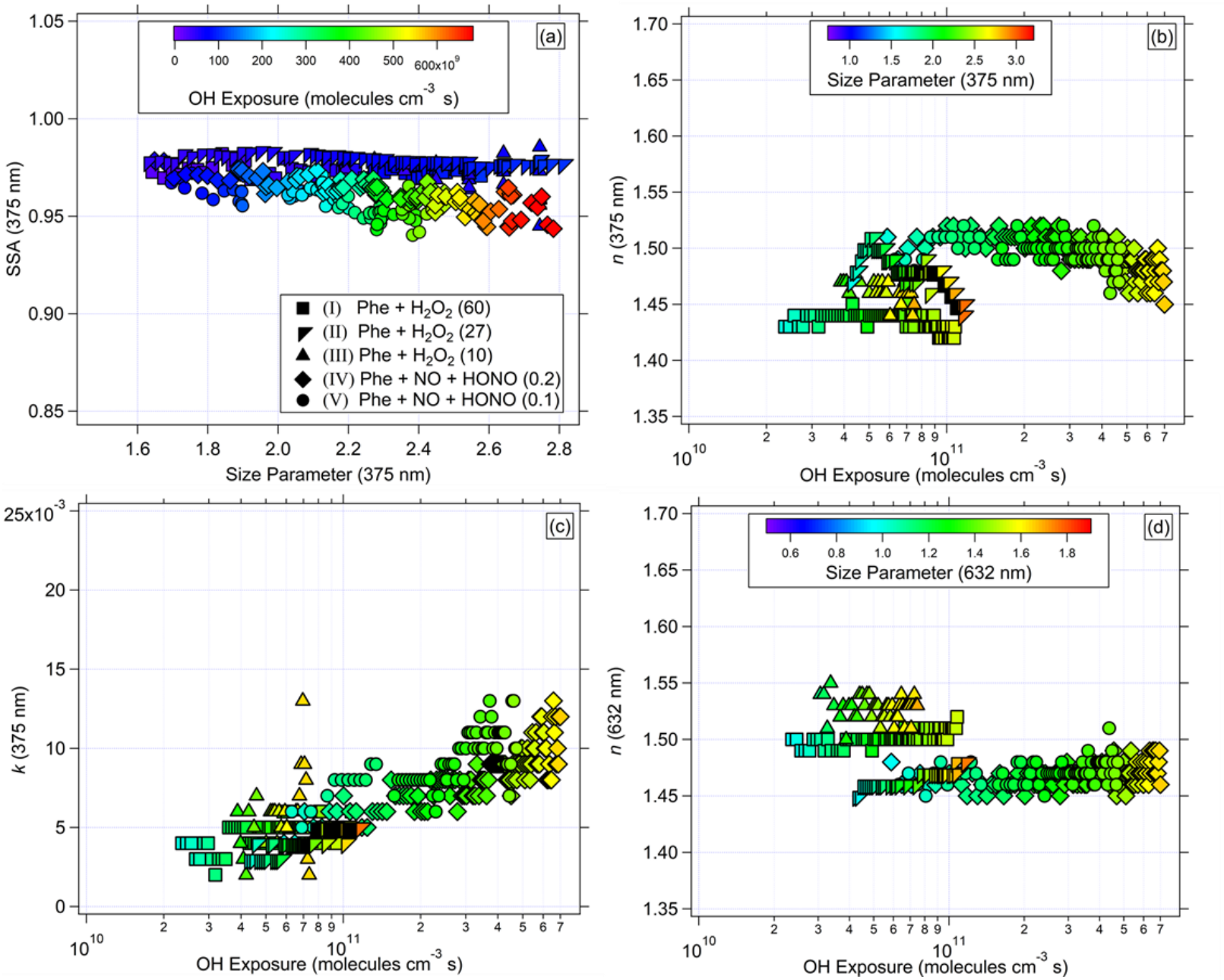

Figure S6. (a) SSA vs. size parameter, and (b) *n* at 375 nm, (c) *k* at 375 nm, and (d) *n* at 632 nm vs OH exposure for longifolene+phenol SOA particles.

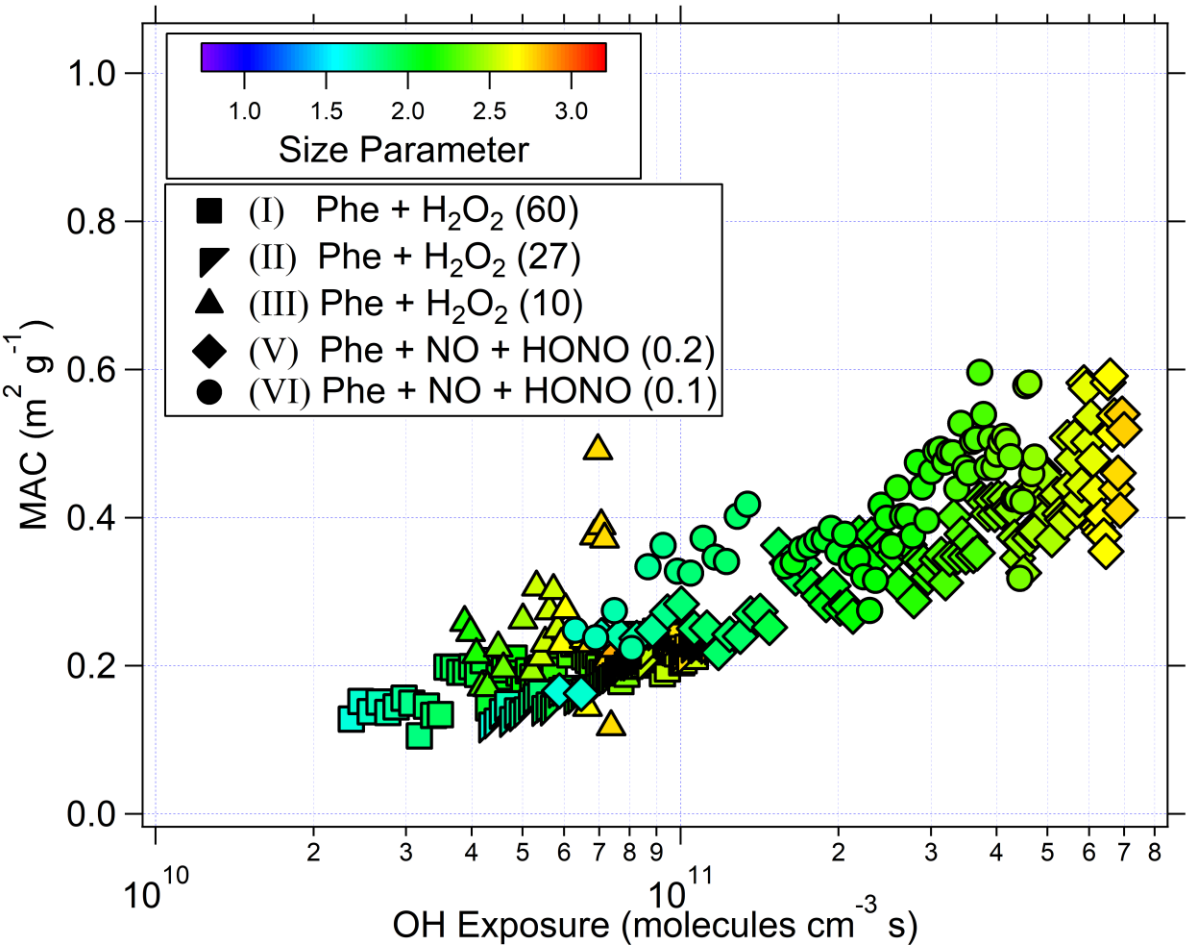

Figure S7. Trends in the derived MAC with OH exposure for longifolene+phenol SOA particles.

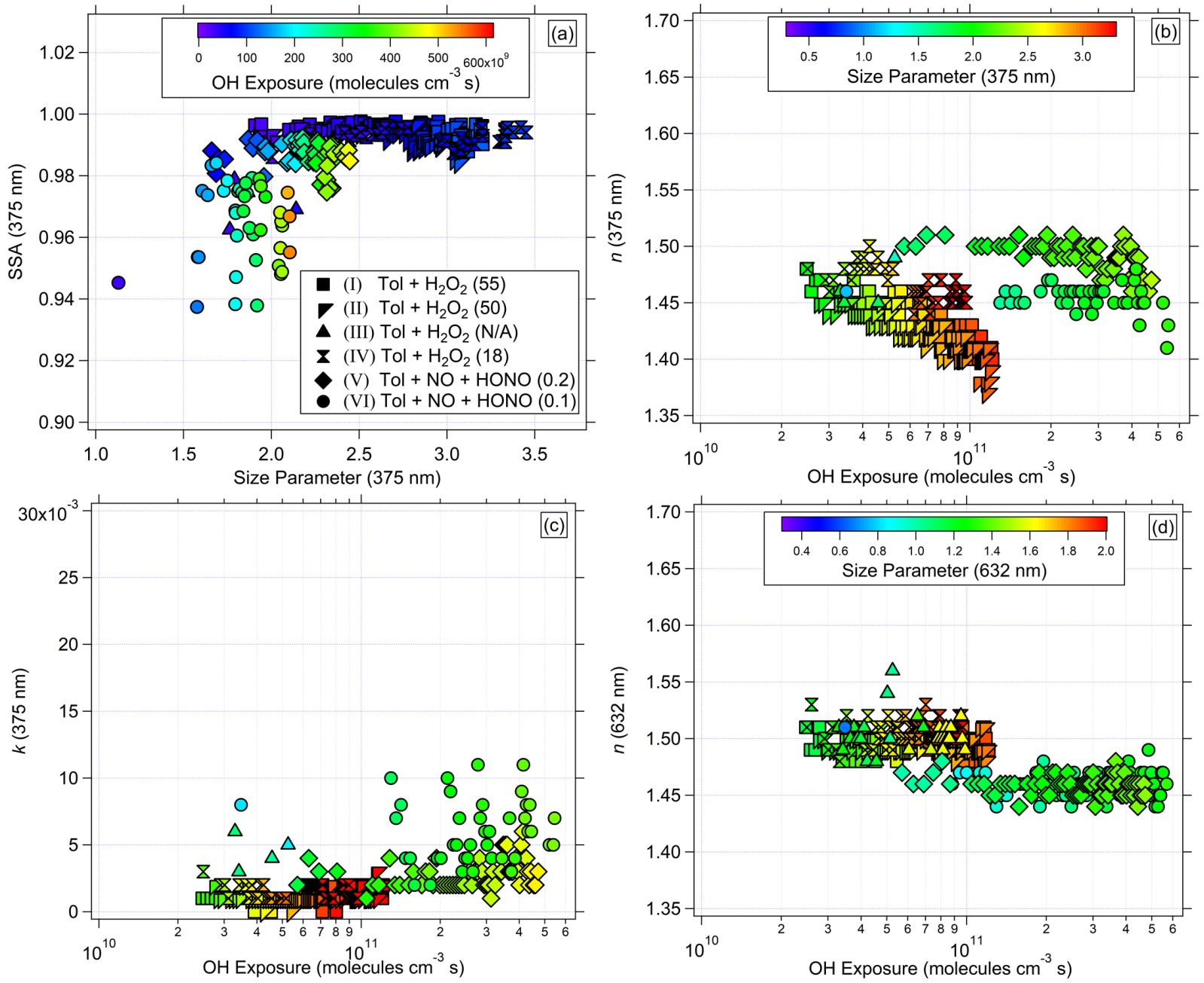

Figure S8. (a) SSA vs. size parameter, and (b) *n* at 375 nm, (c) *k* at 375 nm, and (d) *n* at 632 nm vs. OH exposure for longifolene+toluene SOA particles.

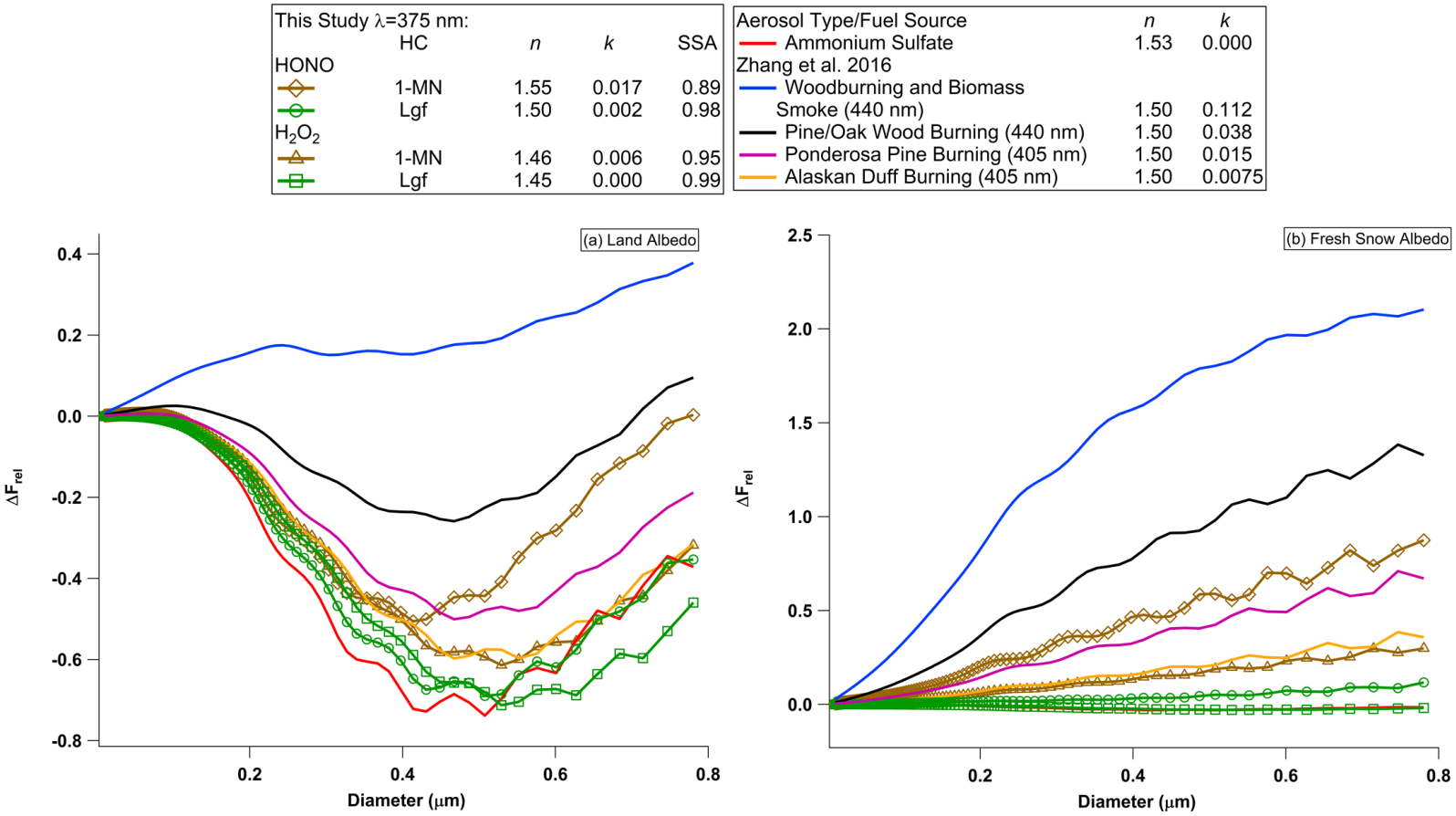

Figure S9. Relative radiative forcing calculated for different RI values as a function of aerosol size and surface albedo. (a) global mean land surface albedo, $\alpha = 0.26$, and (b) fresh snow surface albedo, $\alpha = 0.85$.

References

Bahreini, R., M. D. Keywood, N. L. Ng, V. Varutbangkul, S. Gao, R. C. Flagan, J. H. Seinfeld, D. R. Worsnop, and J. L. Jimenez. 2005. Measurements of Secondary Organic Aerosol from Oxidation of Cycloalkenes, Terpenes, and m-xylene using an Aerodyne Aerosol Mass Spectrometer. *Environmental Science & Technology* 39 (15):5674-5688. doi: 10.1021/es048061a.

Bluvshtein, N., J. M. Flores, Q. F. He, E. Segre, L. Segev, N. N. Hong, A. Donohue, J. N. Hilfiker, and Y. Rudich. 2017. Calibration of a Multi-Pass Photoacoustic Spectrometer Cell using Light-Absorbing Aerosols. *Atmospheric Measurement Techniques* 10 (3):1203-1213. doi: 10.5194/amt-10-1203-2017.

DeCarlo, Peter F., Jay G. Slowik, Douglas R. Worsnop, Paul Davidovits, and Jose L. Jimenez. 2004. Particle Morphology and Density Characterization by Combined Mobility and Aerodynamic Diameter Measurements. Part 1: Theory. *Aerosol Science and Technology* 38 (12):1185-1205. doi: 10.1080/027868290903907.

Langridge, Justin M., Daniel Lack, Charles A. Brock, Roya Bahreini, Ann M. Middlebrook, J. Andrew Neuman, John B. Nowak, Anne E. Perring, Joshua P. Schwarz, J. Ryan Spackman, John S. Holloway, Ilana B. Pollack, Thomas B. Ryerson, James M. Roberts, Carsten Warneke, Joost A. de Gouw, Michael K. Trainer, and Daniel M. Murphy. 2012. Evolution of Aerosol Properties Impacting Visibility and Direct Climate Forcing in an Ammonia-rich Urban Environment. *Journal of Geophysical Research: Atmospheres* 117 (D21). doi: 10.1029/2011jd017116.

Macdonald, F., and D. R. Lide. 2003. CRC Handbook of Chemistry and Physics: From Paper to Web. *Abstracts of Papers of the American Chemical Society* 225:U552-U552.

McComiskey, A., S. E. Schwartz, B. Schmid, H. Guan, E. R. Lewis, P. Ricchiazzi, and J. A. Ogren. 2008. Direct Aerosol Forcing: Calculation from Observables and Sensitivities to Inputs. *Journal of Geophysical Research-Atmospheres* 113 (D9): D09202. doi: 10.1029/2007jd009170.

Moosmüller, H., and W. P. Arnott. 2009. Particle Optics in the Rayleigh Regime. *Journal of the Air & Waste Management Association* 59 (9):1028-1031. doi: 10.3155/1047-3289.59.9.1028.

Nakayama, T., H. Suzuki, S. Kagamitani, Y. Ikeda, A. Uchiyama, and Y. Matsumi. 2015. Characterization of a Three Wavelength Photoacoustic Soot Spectrometer (PASS-3) and a Photoacoustic Extinctiometer (PAX). *Journal of the Meteorological Society of Japan* 93 (2):285-308. doi: 10.2151/jmsj.2015-016.

Taylor, John R. 1997. *An Introduction to Error Analysis: The Study of Uncertainties on Physical Measurements*. Second ed: University Science Books.

Toon, O. B., J. B. Pollack, and B. N. Khare. 1976. Optical Constants of Several Atmospheric Aerosol Species: Ammonium Sulfate, Aluminium Oxide, and Sodium Chloride. *Journal of Geophysical Research-Oceans and Atmospheres* 81 (33):5733-5748. doi: 10.1029/JC081i033p05733.

Ugelow, M. S., K. J. Zarzana, D. A. Day, J. L. Jimenez, and M. A. Tolbert. 2017. The Optical and Chemical Properties of Discharge Generated Organic Haze using In-situ Real-time Techniques. *Icarus* 294:1-13. doi: 10.1016/j.icarus.2017.04.028.